



Scintillation Arcs in Pulsar B0450–18

Barney J. Rickett¹ , Dan R. Stinebring² , Hengrui Zhu² , and Anthony H. Minter³ 

¹University of California, San Diego, CA 92093, USA; bjrickett@ucsd.edu

²Department of Physics & Astronomy, Oberlin College, Oberlin, OH 44074, USA

³Green Bank Observatory, P.O. Box 2, Green Bank, WV 24944, USA

Received 2020 August 5; revised 2020 November 5; accepted 2020 November 10; published 2021 January 27

Abstract

We report on Green Bank Telescope observations of interstellar scintillation from the pulsar B0450–18 at 340 and 825 MHz, revealing prominent arcs in the secondary spectra at both frequencies. The arcs are successfully modeled by one-dimensional angular brightness distributions, estimated by two independent techniques. The distributions do not follow the expected shape for a Kolmogorov plasma density spectrum, and their overall angular widths follow a scaling law, versus frequency, that is slightly slower than the inverse square law expected from plasma dispersion. They also exhibit discrete peaks that are the cause of the occasional reverse sub-arcs. Over a narrow (5%) frequency range these peaks do not participate in the overall spreading, having angular positions that are fixed on the sky. However, the peaks do evolve over a wider range of frequencies and cannot be traced from 825 to 340 MHz. Our conclusions add further evidence for a widespread distribution of highly localized regions of interstellar plasma with small-scale structure that is either elongated or flattened.

Unified Astronomy Thesaurus concepts: [Interstellar medium \(847\)](#); [Interstellar plasma \(851\)](#); [Interstellar scintillation \(855\)](#); [Radio pulsars \(1353\)](#)

1. Introduction

We have found prominent scintillation arcs in radio observations of the pulsar B0450–18, as part of a survey for arcs in 18 pulsars of low to intermediate dispersion measure (DM). B0450–18 lies at about 400 pc distance and -34° Galactic latitude toward the Galactic anti-center (217° longitude) and has $DM = 39.9 \text{ pc cm}^{-3}$. Observations at both 340 and 825 MHz show a clear forward arc, which at 825 MHz is modulated by discrete reverse arcs similar to those observed in B0834+06 and B1737+13 (Stinebring et al. 2001; Walker et al. 2004; Cordes et al. 2006).

At the time of the discovery of parabolic arcs (Stinebring et al. 2001), interstellar scintillation (ISS) was well known and interpreted as due to radio-wave scattering in the interstellar plasma that became ever-stronger with increasing DM. Scattering in discrete regions such as the Crab Nebula, the Vela supernova remnant, and others was well-studied and was incorporated into Galactic electron density models from the mid-1980s onward. However, despite this appreciation of localized scattering, much theoretical and interpretive work envisioned a volume-filling turbulent plasma, whose density followed an isotropic Kolmogorov wavenumber spectrum. The precise parabolic shapes, observed as arcs in the secondary spectra, upset that paradigm as they can only be understood as due to a localized concentration of plasma turbulence occupying only a small fraction of the path from the pulsar. The key idea is the interference between pairs of scattered rays with relative differences in delay and Doppler shift. Parabolic arcs show a quadratic relation between delay and Doppler shift, which can only happen when the rays are all scattered at a common distance.

The observed arcs have been successfully modeled by a phase screen caused by a thin layer of inhomogeneous plasma. The waves that emerge from a phase screen can be described by an angular spectrum or in terms of a brightness power spectrum versus angle. We make use of this concept, which for a single screen is connected to the secondary spectrum by a

double integral over all possible pairs of interfering angles in Equation (8) of Cordes et al. (2006). The integral further collapses to a simple form in the one-dimensional limit of a highly anisotropic brightness function.

However, there remains an open question as to how to reconcile the DM-dependent ISS with the discrete regions implied by arcs. The survey for arcs, mentioned above, is partly motivated by such a question. To our knowledge there has not been a published theoretical analysis of the form of the secondary spectrum expected from scattering that is distributed uniformly along the propagation path. Nevertheless, it is clear that the tight quadratic relation between the differential delay and Doppler shift breaks down for distributed scattering and one expects contours of power in the secondary spectrum, near where the delay is zero, to bulge out in Doppler instead of the narrowing that occurs for a parabolic arc.

In a few nearby pulsars multiple arcs have been observed (Putney & Stinebring 2006), in which there are two or three clearly distinguished narrow parabolic arcs with different curvatures. The theory for such a case has been developed by Simard et al. (2019), who give an analysis of arcs from two screens, and applied it to the arc observations of B0834+06 by Brisken et al. (2010).

In the context of the increasing strength of ISS with DM, the Galactic distribution of interstellar plasma must include a widespread distribution of clumps with enhanced plasma density and turbulence. There are now several models for the Galactic distribution of plasma density (e.g., Cordes & Lazio 2003; Yao et al. 2017). These include some discrete concentrations such as in H II regions and supernova remnants embedded in a smooth plasma distribution and even occasional voids like the Local Bubble and regions dominated by very high-temperature “coronal” plasma. Several authors (e.g., Gupta et al. 1999) have speculated that plasma at the boundary of the Local Bubble (and more typical interstellar medium conditions) is a potential site for a scattering screen.

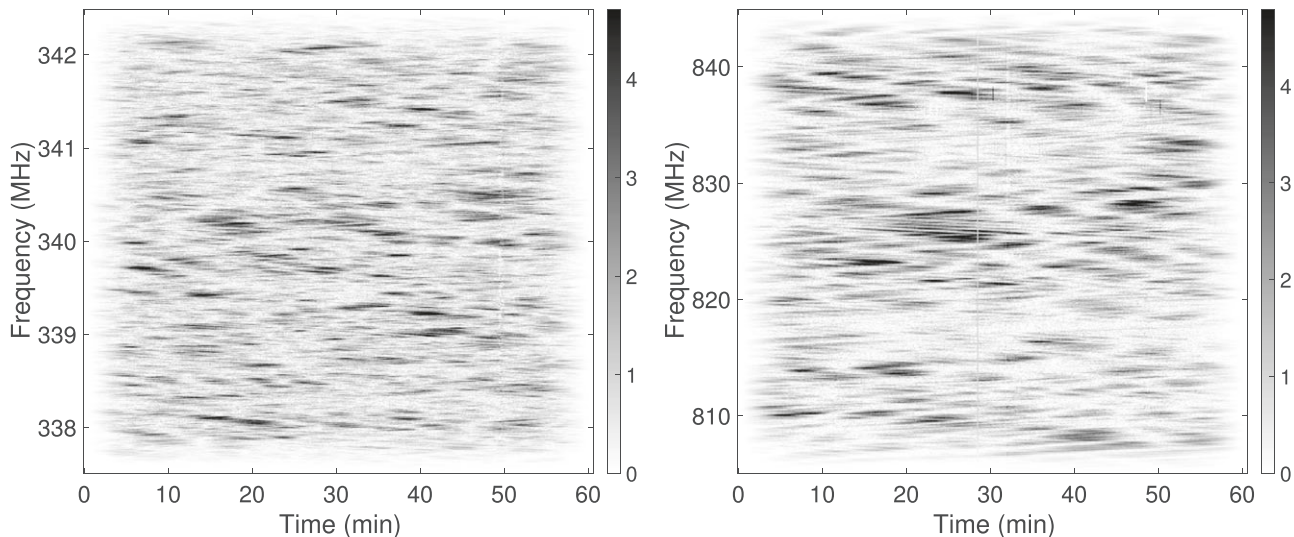


Figure 1. Dynamic spectrum of interstellar scintillation observed at the Green Bank Telescope from pulsar B0450–18. Left: MJD 53632 at 340 MHz. Right: MJD 53637 at 825 MHz. The grayscale units are linear as a fraction of the mean pulsar flux density.

The distance and DM of our pulsar B0450–18 correspond to a mean density of $0.1 \text{ electrons cm}^{-3}$, which is about five times that typical on sightlines to nearby pulsars. This suggests a localized concentration of electrons, and we proceed by adopting such a thin-screen model for the arcs we report here.

2. Observations, Dynamic and Secondary Spectra

The Green Bank Telescope was used in 2005 to survey DM $< 50 \text{ pc cm}^{-3}$ pulsars at frequencies of 340 and 825 MHz. A paper describing the survey and the results is in process (D. R. Stinebring et al. 2021, in preparation). Here we report particularly interesting scintillation arcs from pulsar B0450–18. We used the Spectral Processor backend, which produced spectral estimates of 1024 channels about every 1 ms. In post-processing, these spectra were averaged synchronously with the pulsar period in ON and OFF gates for 10 s, and then an ON–OFF dynamic spectrum was formed and corrected for bandpass effects by dividing by the average spectrum over the observation in a standard fashion (Hill et al. 2005). Additionally, we performed standard post-detection dispersion removal and corrected for the full bandwidth modulation due to intrinsic short-term pulse amplitude variations averaged over the 10 s sample time. Modest radio-frequency interference in the dynamic spectrum was removed by inspection and replaced with adjacent spectral samples.

The pulsar was observed at 340 MHz (bandwidth of 5 MHz) on MJD 53632 and at 825 MHz (bandwidth of 40 MHz) for one hour on 53637. The dynamic spectra are displayed in Figure 1. They have high signal-to-noise ratio and well-resolved “scintle” structure in frequency and time. As elaborated upon below, although the field of scintles appears fairly random in frequency and time, there is an underlying order to their structure at both frequencies that is indicative of scattering confined to a thin screen.

We computed the Fourier transforms of the dynamic spectra over both time and frequency in the usual fashion (e.g., Stinebring et al. 2019). The modulus squared of the Fourier transform gives the secondary spectra $S_2(\tau, f_D)$, where τ is the delay (conjugate to frequency in the dynamic spectrum) and f_D is the Doppler frequency (conjugate to time in the dynamic

spectrum). Note that the dynamic spectrum is real and so $S_2(\tau, f_D) = S_2(-\tau, -f_D)$. Figure 2 plots S_2 in dB and the overall shape is emphasized by displaying both positive and negative delays. Since the power is concentrated near the delay axis, we expand in Doppler out to $\pm 25 \text{ mHz}$. On the right side we illustrate how we estimate the parabolic curvature, as described below.

We also note that the logarithmic display allows one to see a wide dynamic range and that the arcs are more than 20 dB below the peak near the origin. This peak would dominate a linear display, and its half-power widths would describe the ISS by the reciprocal of the diffractive frequency and timescales.

The distribution of power in Figure 2 outlines parabolic arcs at both frequencies with a deep minimum along the delay axis itself. This is characteristic of very anisotropic scattering. Accordingly, we have fitted models with a 1D brightness distribution $B(\theta)$ where θ is the scattered angle and $\theta_x = \theta \cos \psi$ is the angle projected parallel to the transverse effective velocity, which defines the x -axis. The transverse proper motion velocity is measured to be about 26 km s^{-1} , based on a distance of about 400 pc (Chatterjee et al. 2009; Jankowski et al. 2019).

We estimated the curvature η of the parabolic arcs, as shown in the right-hand sub-panels of Figure 2. We searched in 50 equi-spaced logarithmic steps over a 100:1 range in η . At each step we computed the sum of $S_2(f_D, \tau)$ along the corresponding parabola. A separate sum was computed from positive and negative Doppler frequencies and covered a fixed range in delay; at each delay we interpolated S_2 at the Doppler frequency lying on the parabola. The range in delay, indicated by the colored rectangles in the left panels, was chosen to emphasize the low-level arcs, made visible by the logarithmic grayscale and also to avoid the peak near the origin where the arc is less well defined. The right-hand panels in Figure 2 show where the parabolic sums peak, marked by short horizontal bars. The overall curvature values were estimated from the average of positive and negative Doppler frequencies: $\eta = 6.3$ and 0.88 s^3 at 340 and 825 MHz, respectively. We refined the curvature estimates during subsequent model fitting and

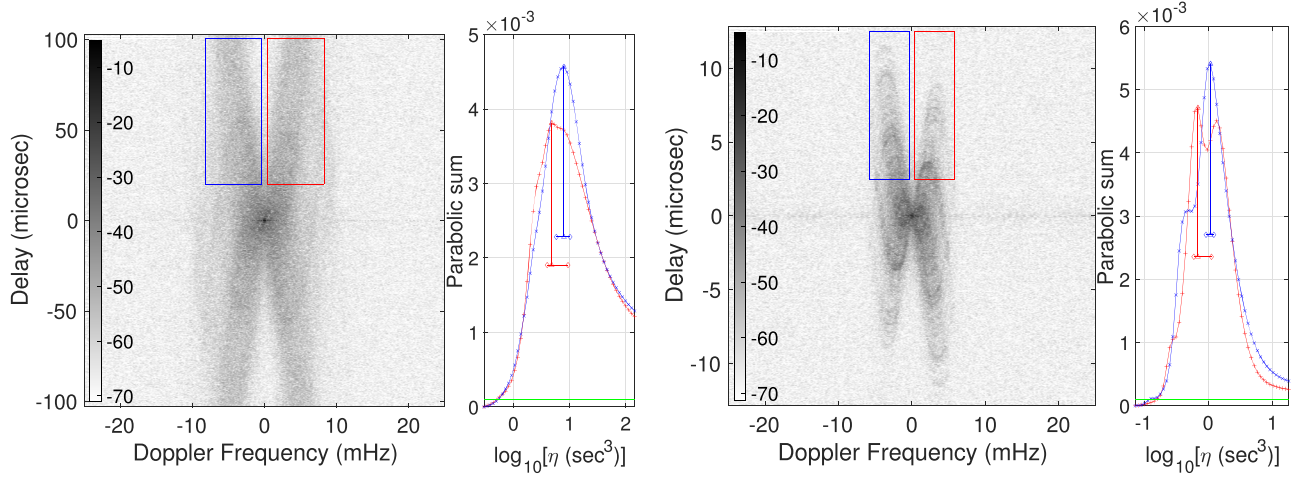


Figure 2. Secondary spectrum S_2 (in dB) of interstellar scintillation observed at Green Bank Telescope from pulsar B0450–18. Left: MJD 53632 at 340 MHz. Right: MJD 53637 at 825 MHz. Since S_2 is only significant near the delay axis, we expand the left sub-panels about ± 25 mHz (half the Doppler Nyquist frequency). We include positive and negative delays to reveal the structure near the origin. The right sub-panels plot the parabolic sum of S_2 vs. curvature for positive (red) and negative (blue) f_D ; the summation is linear and is confined to the areas inside the red and blue rectangles of the S_2 plot. The peaks in the sum determine the chosen curvature, which are marked by a vertical line and a horizontal bar marking where the sum is above 95% of the peak.

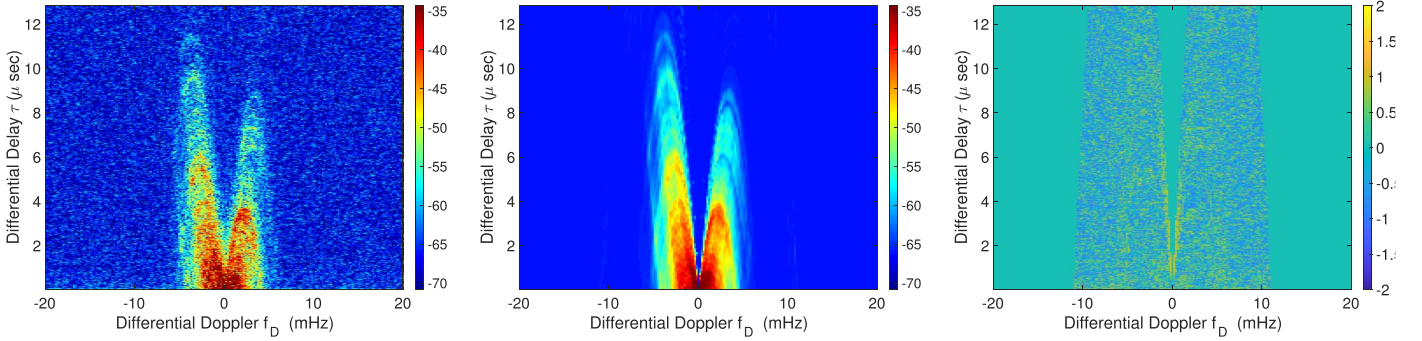


Figure 3. Secondary spectrum (in dB) of interstellar scintillation at 825 MHz from B0450-18 on MJD 53637. Left: observation; middle: 1D model; right: normalized residual = (observation–model)/model.

adopted the following values: $\eta = 4.77$ and 0.81 s^3 , at 340 and 825 MHz, respectively.

3. 1D Model for Brightness Distribution

Assuming a 1D brightness distribution, we fitted models to the secondary spectrum using two methods. The mapping from the sky coordinates to the secondary spectrum was presented in Stinebring et al. (2019), and we refer the reader to that paper for the basic theory. We repeat their Equation (5) below, which gives $S_2(f_D, \tau)$ as the product of the brightness $B(\theta)$ arriving from the two interfering angles:

$$S_2(f_D, \tau) = B(\theta_+) B(\theta_-) / |2\sqrt{\eta}f_D|, \quad (1)$$

$$\text{with } \theta_{\pm} = \sqrt{\frac{2c}{D_{\text{eff}}}} \beta_{\pm}, \quad (2)$$

$$\text{and where } \beta_{\pm} = \frac{1}{2}[-\tau/(\sqrt{\eta}f_D) \pm \sqrt{\eta}f_D]. \quad (3)$$

Here we define:

$$\eta = \frac{cD_{\text{eff}}}{2\nu^2V_{\psi}^2}, \quad D_{\text{eff}} = D_{\text{psr}}(1-s)/s, \quad (4)$$

$$V_{\psi} = |V_{\text{eff}}| \cos \psi, \quad (5)$$

$$\text{and } V_{\text{eff}} = [(1-s)V_{\text{psr}} + sV_{\text{obs}} - V_{\text{scr}}]/s, \quad (6)$$

where s is the distance from pulsar to screen as a fraction of the distance from pulsar to observer (D_{psr}). V_{psr} is the proper motion velocity of the pulsar, V_{obs} is the observer transverse velocity, and V_{scr} is the screen transverse velocity.

3.1. Iterative Least-squares Fitting

In our first method, we specify an initial brightness profile at a set of discrete angles β , which are related to the observed angles θ by Equation (2). With this definition the relative delay at that angle is $\tau = \beta^2$ independent of the radio frequency, so expressing delay in microseconds makes the units of β the square root of microseconds. Consider 825 MHz: the forward arc extends to about $\tau_{\text{max}} \sim 10 \mu\text{s}$, and β was fitted over $\pm\beta_{\text{max}}$, which we set to $\pm 5 \mu\text{s}^{0.5}$ extending in delay beyond τ_{max} to $\tau = 25 \mu\text{s}$.

We calculate the model $S_2(f_D, \tau)$ from Equation (1) with the addition of a constant noise level. We used an iterative non-linear fitting of the brightness model to minimize the mean-squared difference between the model and the observation. Given the exponential distribution expected for the observed spectral density, the rms fluctuation at each pixel should equal its mean; consequently we divided the residual by the larger of the model and the observation.

In Figure 3 we compare the 825 MHz observed and model secondary spectrum and also show the residual fractional

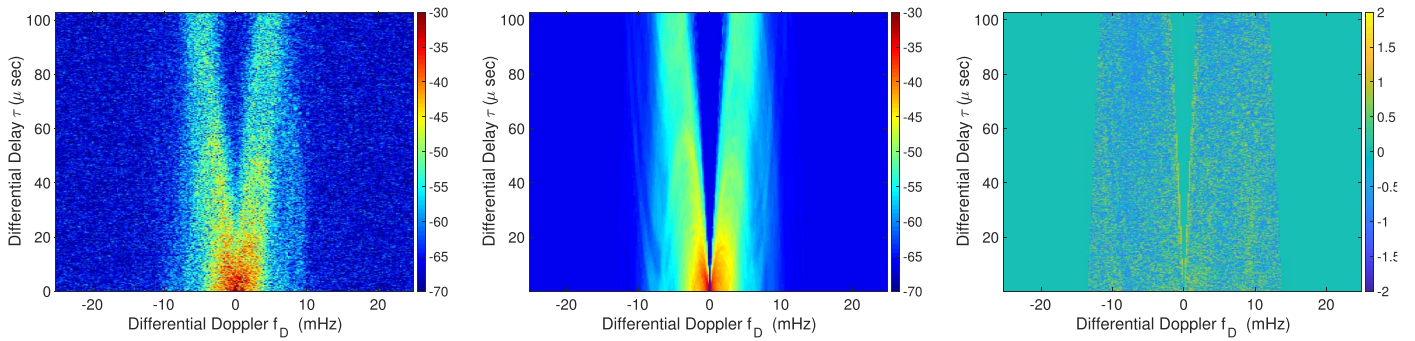


Figure 4. Secondary spectrum (in dB) of interstellar scintillation at 340 MHz from B0450–18 on MJD 53632. Left: observation; middle: 1D model including the first alias in delay; right: normalized residual = (observation–model)/model.

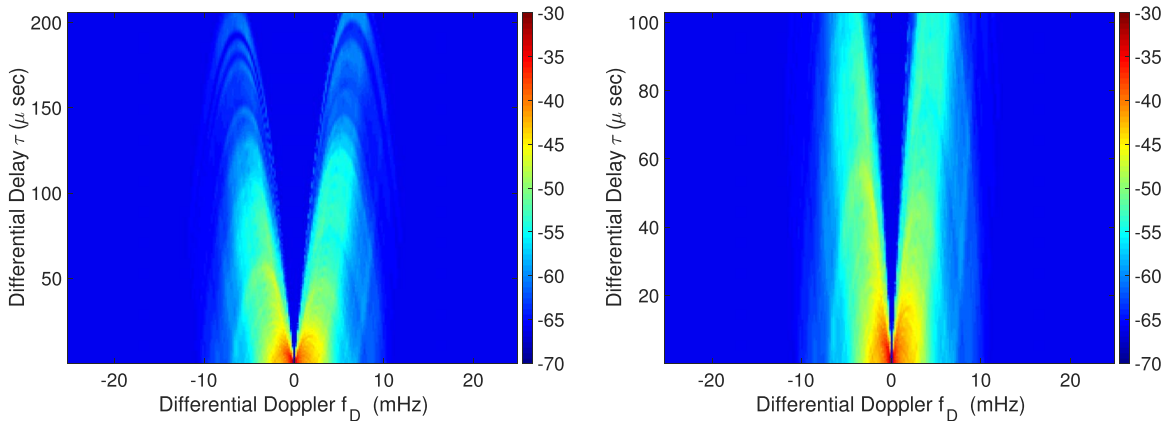


Figure 5. Left panel shows a 1D model for secondary spectrum (in dB) of interstellar scintillation at 340 MHz from B0450–18 calculated out to twice the Nyquist delay in the observations. The right panel shows $S_2(f_D, \tau)$ without adding the power aliased from above the Nyquist delay. It should be compared to the middle panel above in Figure 4; notice the somewhat reduced power in the range 5–10 mHz at delays up to 70 μ s and on the upper parts of the forward arc.

difference between them. The reverse sub-arcs observed are reproduced quite clearly in the model, as evident in the absence of sub-arc structures in the residual plot. In particular, note the arclets whose apexes are near 4 μ s in delay at both positive and negative f_D .

However, the model does exclude the V-shaped region near the delay axis and also at large values of f_D , as indicated in the right panel of Figure 3 where the residual is set to zero (green). The fit is good with low residuals except near the edge of this V-shaped valley. We note that this valley region is where the effects of scattering from a 2D brightness distribution would be first noticeable and do not attempt to widen the 1D fitting range in β , which would narrow the V-shaped region.

Now consider a 1D model for the 340 MHz observations. At this lower frequency the arc structure comprises a prominent broad V-shaped forward arc superimposed by a few faint reverse sub-arcs. We show the observations and fits in the same format as for 825 MHz in Figure 4. The observed forward arc (left panel) extends out to the Nyquist point in delay ($\tau_{\text{nyq}} = 103 \mu$ s), and so we must examine the effect of aliasing from even higher delays.⁴

⁴ Aliasing occurs when a quantity is measured at a sampling rate that is not fast enough to capture its rapid variations. Here the sampling was determined by the frequency and time resolutions in the dynamic spectra. The frequency resolution in the left panel of Figure 1 was 4.9 kHz, but was insufficient to resolve the narrowest features in the spectrum. Consequently features in S_2 at delays above the Nyquist delay $\tau_{\text{nyq}} (= 1/(2 \cdot 4.9 \text{ kHz}) = 103 \mu$ s) will appear aliased to delays within the range $\pm 103 \mu$ s. With our 2D measurement there is no aliasing in Doppler, for which the Nyquist frequency is 50 mHz.

Consequently we created model secondary spectrum out to 206 μ s—twice the Nyquist delay. We used a range $\pm \beta_{\text{max}}$ with $\beta_{\text{max}} = 20 \mu\text{s}^{0.5}$, which would allow for reverse arcs with apexes to 400 μ s. An example is shown in the left panel of Figure 5. The first alias in delay is a shift to $\tau - 2\tau_{\text{nyq}}$ which is negative. Since S_2 is Hermitian and we only fit positive delays, we add its contribution at $S_2(-\tau + 2\tau_{\text{nyq}}, -f_D)$. We coded this into the model computation routine and used it to fit the observed $S_2(f_D, \tau)$. The overall fitted model and its residuals are in the middle and right panels of Figure 4.

Close examination of the observation in the left panel shows broad low-level power at $f_D = 5\text{--}10$ mHz extending from 0 to at least 70 μ s. This is more obvious at positive than at negative Doppler frequencies and the middle panel shows that it is successfully modeled, including the effects of aliasing. We estimate a reduced $\chi^2 = 0.83$ by summing the squares of the residuals normalized by the model and dividing by the number of degrees of freedom (excluding green pixels which are not reached by the model). This implies that the rms error at each pixel is somewhat less than the model itself, and we conclude that the overall fit is satisfactory.

In Figure 6 we overplot the brightness models at both frequencies with their error bars at $\pm 1\sigma$. As in Stinebring et al. (2019), we plot brightness versus angle θ . The scaling from β (units $\mu\text{s}^{0.5}$) depends on the pulsar distance and s the unknown fractional screen-to-pulsar distance. With our pulsar at 400 pc and converting θ into mas the relation becomes $\theta_{\text{mas}} = 1.44 \beta \sqrt{s/(1-s)}$. For simplicity, throughout the rest

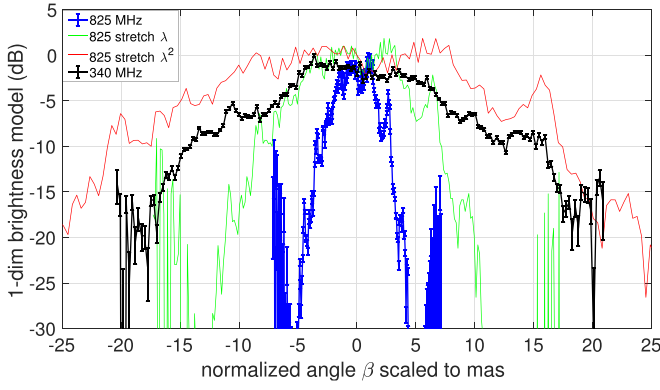


Figure 6. 1D brightness models at 340 MHz and at 825 MHz vs. β with $\pm 1\sigma$ error bars. The 825 MHz model is also stretched in β to 340 MHz by the wavelength ratio to the power of 1 and 2.

of the paper we display angular distributions in mas assuming a mid-placed screen ($s = 0.5$).

Evidently, the profile at 340 MHz is much wider than at 825 MHz. At the lower frequency there is a significant offset peak near $+15$ mas ($\beta = 11 \mu\text{s}^{0.5}$), which causes a reverse arclet with an apex at 5 mHz and $121 \mu\text{s}$. Since this is beyond the Nyquist delay, the apex cannot be seen in the secondary spectrum. It does, however, account for the bulge in power, mentioned above, at $f_D = 5\text{--}10$ mHz and $\tau \approx 0\text{--}70 \mu\text{s}$. Its apex is aliased to -5 mHz and $86 \mu\text{s}$, and so contributes power to the top left side of the forward arc. Given that we include estimates the brightness function beyond the Nyquist delay, we note that the effects of aliasing are significant. However, they are at a low level as can be seen by comparing the full aliased model in the middle panel of Figure 4 with the model without the aliased power in the right panel of Figure 5. Consider, for example, the faint arclets with apexes $180\text{--}200 \mu\text{s}$ on the right side before aliasing. They contribute broadening on the left side at delays of $6\text{--}26 \mu\text{s}$ as the tails of forward parabolic arclets. In summary, we are confident in identifying the offset peak near 15 mas, which is significant relative to the errors over about 10 pixels. However, the lower-level (± 1 dB) peaks in brightness in the entire range between ± 20 mas are comparable to the errors.

3.2. $\theta\text{--}\theta$ Mapping Estimate of Brightness Distribution

While the iterative least-squares fitting gives a satisfactory representation of the secondary spectrum, the technique can sometimes result in a local chi-squared minimum instead of the global one. Here, we present a novel estimation technique from a non-iterative $\theta\text{--}\theta$ mapping (D. Baker et al. 2021, in preparation; Sprenger et al. 2021) and show the consistency between the two methods. We map the coordinates from f_D, τ into the sky angles θ_{\pm} given in Equation (3) as follows:

$$f_D(\theta_+, \theta_-) = \frac{V_{\psi}}{\lambda}(\theta_+ - \theta_-) = \frac{\beta_+ - \beta_-}{\sqrt{\eta}} \quad (7)$$

$$\tau(\theta_+, \theta_-) = \frac{D_{\text{eff}}}{2c}(\theta_-^2 - \theta_+^2) = \beta_-^2 - \beta_+^2. \quad (8)$$

The resultant mapping is referred to as the $\theta\text{--}\theta$ spectrum $I(\theta_+, \theta_-)$ and is given below, including the Jacobian of the transformation, with the final form obtained from the model of

Equation (1):

$$I(\theta_+, \theta_-) \equiv S_2(f_D, \tau) |2\sqrt{\eta}f_D|, \quad (9)$$

$$= B(\theta_+)B(\theta_-). \quad (10)$$

Note that, by its definition, $I(\theta_+, \theta_-)$ is ensured to be Hermitian. Intuitively, in the regime of 1D scattering, the $\theta\text{--}\theta$ spectrum encodes the intensity of the interference from all pairs of subimages, i.e., θ_+ and θ_- . Under such a mapping, an inverted arclet, formed by one subimage at θ_0 interfering with the rest (Walker et al. 2004; Walker & Stinebring 2005; Brisken et al. 2010; Simard & Pen 2018), is mapped to two mutually orthogonal straight lines: $\theta_+ = \theta_0$ and $\theta_- = \theta_0$.

The resulting $\theta\text{--}\theta$ spectrum at 825 MHz is presented in the left panel of Figure 7. It defines $I(\theta_+, \theta_-)$ in a square region bounded by $\pm\theta_{\text{max}} = \sqrt{2c\tau_{\text{nyq}}/D_{\text{eff}}}$, where $\tau_{\text{nyq}} = 12.8 \mu\text{s}$ is the Nyquist value in delay.

Considering a square region as in Figure 7, we can write an eigenvalue equation for $I(\theta_+, \theta_-)$. We solve for $B(\theta)$ as its first eigenvector and show the corresponding model, the outer product of $B(\theta)$ with itself, in the middle panel. Notice that the noise floor is no longer uniform in the observed $\theta\text{--}\theta$ spectrum (left panel) because of the extra scaling by the Jacobian through the mapping Equation (9). So we estimate the noise floor from a region in the secondary spectrum far from any scintillation signature and remove it from the observed spectrum before solving for the eigenvector. The noise floor is then added back into the model. We then compute the residual difference between the observed mapping $I(\theta_+, \theta_-)$ and this model. The right panel shows the residual normalized, as in Section 3.1, by the maximum of the data and model at each pixel.

If the scattered image is truly one-dimensional, then Equation (10) implies that the $\theta\text{--}\theta$ spectrum becomes the outer product of the brightness function with itself. Such a spectrum has only one eigenvector, namely the brightness function multiplied by a scaling factor. Hence, in the case of highly anisotropic scattering, the $\theta\text{--}\theta$ estimate becomes uniquely defined.

In the 825 MHz $\theta\text{--}\theta$ spectrum (left panel of Figure 7), notice that the arclets are not mapped to exactly straight horizontal and vertical lines: there are some hyperbolic streaks near the diagonal $\theta_+ = \theta_-$. Such streaks are due to the change in pixel shape through the mapping. A rectangular pixel in the secondary spectrum is mapped to a region bounded by two hyperbolas (constant τ) and two lines parallel to the diagonal $\theta_+ = \theta_-$ (constant f_D), according to Equations (7) and (8), which makes a highly elongated shape parallel to the diagonal. However, since we define rectangular pixels in $\theta\text{--}\theta$ space, the mapping can cause multiple $\theta\text{--}\theta$ pixels to originate from a single pixel in the secondary spectrum. Consequently, in these regions $\theta\text{--}\theta$ pixels are not independent of each other, but can be highly correlated along the diagonal, seen as the streaking. Fortunately, the streaks are most visible where the scintillation signal in the secondary spectrum is at a low level, so that they are not very prominent in the residual plot. Thus they do not concern us any further in this work.

We also note that near the diagonal $\theta_+ = \theta_-$ (where $|f_D|$ is small) the $\theta\text{--}\theta$ map extends out to considerably larger θ values than θ_{max} , which defines the rectangular range plotted in Figure 7. It is evident that angles larger than θ_{max} map to the V-shaped region in the secondary spectrum that could not be modeled by a finite range in angle.

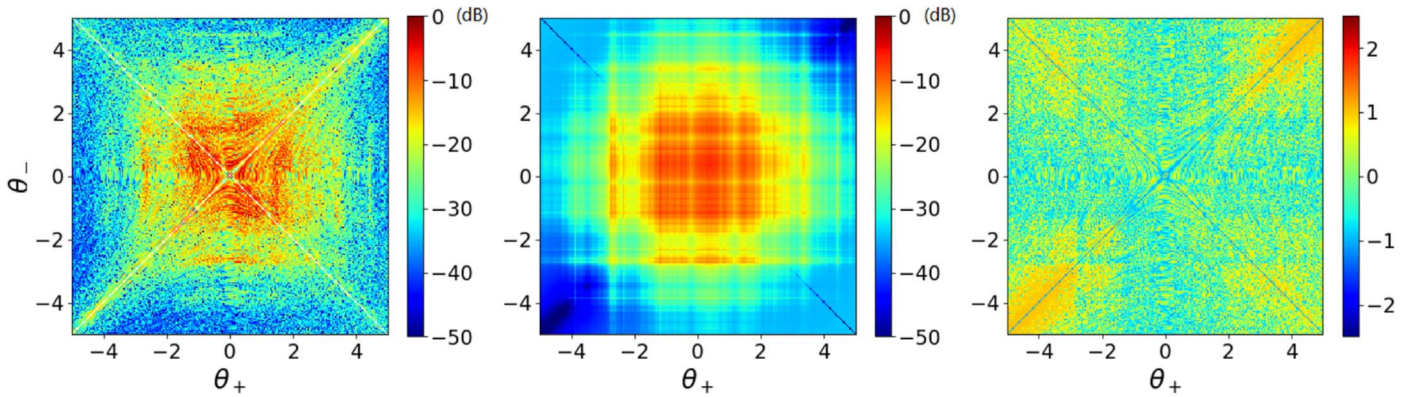


Figure 7. θ - θ spectrum of interstellar scintillation at 825 MHz from B0450-18 on MJD 53637 in decibel vs. angle in mas. Left: observation; middle: outer product of the 1D model + mean of noise; right: fractional residual = (observation-model)/max(observation,model).

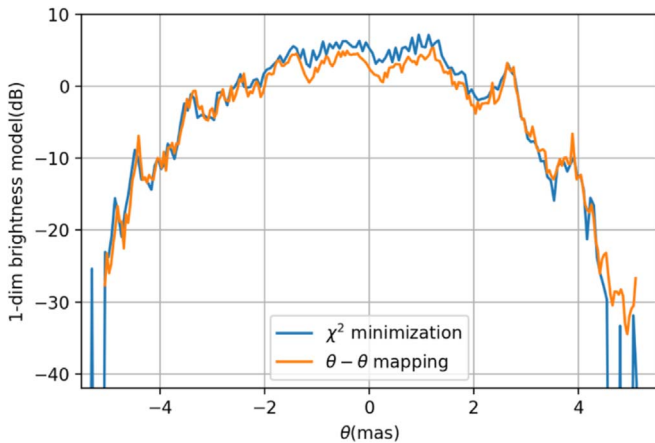


Figure 8. Two brightness models at 825 MHz overplotted in decibel vs. angle β scaled to mas assuming a midpoint screen distance.

In Figure 8, we compare the 1D models from the two methods for the 825 MHz data. (We do not apply the θ - θ mapping to the 340 MHz observations because of the significant aliasing discussed in Section 3.1.) The models are normalized by their means to best demonstrate the alignment. The overall agreement between the two models is satisfactory, except near the origin. By the argument above regarding the change of pixel shape through the mapping, the effective pixel shape becomes wider in the θ - θ spectrum near the origin, which causes the offsets near the origin. Overall, the basic features of the 1D brightness profiles are reproduced by both methods, reinforcing our confidence in the modeling.

4. Wavelength Scaling of Brightness Profiles

We now compare the model brightness profiles fitted at 340 and 825 MHz. The observations were five days apart, which at the 26 km s^{-1} proper motion speed of the pulsar causes an angular difference of 0.2 mas between the observations. This is small compared to the 3 mas width in brightness at 825 MHz, and so we assume that there were negligible time variations over the five days. The profiles are both computed versus normalized angle β , which does not depend on the central observing wavelength as defined in Equation (3). In Figure 6 we overplot the 1D fitted brightness profiles from 340 MHz in black and from 825 MHz in blue, after scaling β into mas, as noted above.

If the interstellar scattering region responsible had homogeneous random 1D variations in electron density, we would expect the widths in brightness to scale as λ^a with $a = 2$ or 2.2 for a Gaussian or Kolmogorov wavenumber spectrum, respectively. For comparison we show the 825 MHz models stretched in angle according to linear (green) and square law (red) wavelength scaling laws.

The 340 MHz profile has a relatively flat top dropping abruptly above +6 and below -5 mas; from here it falls by about 20 dB to the edge of the modeled range. The comparison with 825 MHz is not consistent with a single scaling exponent a . Though the central region is also flat at 825 the red ($a = 2$) scaling makes it wider than at 340 MHz. We note also that $a = 2$ gives an apparent alignment of the red and black peaks near +15 mas.

We have attempted to both stretch and shift the two profiles to allow for a plasma refractive shift as well as scatter broadening, but this does not yield a convincing agreement for both the flat tops and the 340 MHz peak at +15 mas. An alternative estimate of the width is the equivalent width, defined as the width of a rectangle with the same area as that under the fitted brightness: $\theta_{\text{equiv}} = \int B(\theta) d\theta / B_{\text{max}}$. At 340 and 825 MHz, this gives $\theta_{\text{equiv}} = 12.1 \pm 1$ and 2.7 ± 0.3 mas, respectively. This yields an estimated exponent $a = 1.7 \pm 0.2$, where the error is dominated by uncertainty in B_{max} due to the variations in B near the peak.

It should also be noted that the shapes plotted do not follow the expectations of a 1D or 2D Kolmogorov spectrum. These findings follow very similar conclusions to those in our earlier study of arcs in pulsar B1133+16. Wavelength scaling laws shallower than expected have been reported in many other observations of ISS from pulsars (Löhmer et al. 2001, 2004; Bhat et al. 2004; Geyer & Karastergiou 2016; Lewandowski et al. 2015). As an alternative to the random interstellar scattering model for ISS, several authors (Romani et al. 1987; Pen & Levin 2014; Simard & Pen 2018; Gwinn 2019; Gwinn & Sosenko 2019) have advanced discrete plasma structures, often modeled as lenses, as the explanation of scintillation arcs. Few of these models have included wavelength scaling predictions, although Simard & Pen (2018) found Gaussian-profiled lens models that predicted reverse arc locations would be nearly independent of wavelength.

A more thorough analysis of the 825 MHz spectrum shows evidence for narrow-brightness features whose angular positions are nearly independent of frequency. In Figure 9, we analyze the most prominent arclet at around 2.7 mas in the

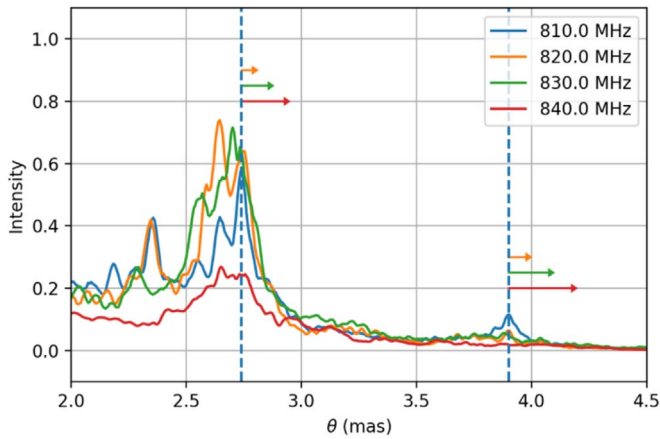


Figure 9. Frequency dependence of the arcslets’ position. The arrows show the expected shifts of the peaks under a λ^2 scaling. While the shapes of individual peaks change significantly, their locations remain nearly independent of frequency.

825 MHz secondary spectrum. The corresponding dynamic spectrum has a total bandwidth of 40 MHz. We divide the spectrum into four chunks in frequency and estimate the brightness function using the θ - θ mapping formalism. The brightness functions centered at four adjacent frequencies are over-plotted in Figure 9 and compared to theoretical predictions of a λ^2 scaling as indicated by the arrows. While the shape of the 1D brightness profile undergoes substantial changes even across 40 MHz of bandwidth, we see that the two local maxima, labeled with blue dashed lines, remain in essentially the same sky position as a function of frequency, in accord with the similar result in Hill et al. (2005); at the very least, the arcslets do not show evidence of participating in the predicted λ^2 scaling of the overall profile.

In summary, we see dramatically different frequency scaling in the overall $B(\theta)$ profile width compared to the behavior of discrete, localized maxima.

5. Wavelength Scaling of the Visibility Function

The Fourier transform of $B(\theta)$ gives an estimate for the visibility function of the field as it leaves the scattering screen, which is where there is a purely phase-modulated wave front. This quantity $\Gamma_\lambda(s_d)$ is a function of the spatial offset (baseline). In the Appendix we show that for plasma scattering, in the limit of small spatial offsets, the form of $\Gamma_\lambda(s_d)$ is a common function of the offset *times* the wavelength (see Equation (A7)). Note that such a spatial scaling corresponds to λ^2 scaling in the brightness versus angle because the kernel in the transforms, such as in Equation (A4), is $\exp[2\pi j s_d \theta / \lambda]$. Figure 6 compares the brightness estimates at the two frequencies plotted in dB, which makes the low-level peaks at large angles more visible. We emphasize such peaks in our discussion. These peaks contribute to only low-level ripples in the visibility, with spatial periods smaller than the visibility scale at 50%. Thus they do not affect our estimates of this scale very much: $\sigma_{340} = 5.3 \pm 0.8$ and $\sigma_{825} = 9.3 \pm 1.8$ Mm, respectively (with a constant multiplier that depends on the actual value of the screen distance parameter s). The ratio of the 50% widths is significantly less than the inverse of the wavelength ratio, and in angular widths corresponds to a wavelength exponent $a = 1.7 \pm 0.2$.

6. Discussion

We have observed prominent arcs in the ISS pattern of pulsar B0450–18 at 340 and 825 MHz and have successfully fitted 1D models of the scattered brightness at each frequency. The shapes of these brightness functions do not conform to the predicted ensemble average for a Kolmogorov spectrum of electron density.

6.1. The Width of Scattered Brightness

We over-plotted the two brightness functions to determine a wavelength scaling law but found that no single scale factor matches the shapes accurately. The angular widths defined at, say, 3 dB below the peaks yielded widths $\propto \lambda^a$ with a somewhat less than 2; when characterized by an “equivalent width,” we obtained $a = 1.7 \pm 0.2$. An alternative analysis in the spatial domain reveals a field correlation scale of about 10^7 m, which scales as $\lambda^{-0.7}$ corresponding to an angular width in brightness that scales as $\lambda^{1.7}$. Overall, the comparison confirms that the arcs are indeed due to a highly localized concentration of *plasma* that has very elongated fine structure.

In the Appendix we note that frequency dependence of the screen phase enters explicitly in the spatial domain. It has been common in much of the literature to consider frequency scaling under the hypothesis that an ensemble average will approximate an observed estimate of scattered pulse shape or scattered brightness function for ISS. An ensemble average of the visibility function in Equation (A5) is readily obtained under the reasonable assumption that the screen phase is distributed as a zero mean random variable with Gaussian statistics. This leads to the well known result which is noted following the Equation (A5) in the Appendix. Then the scaling law depends on the mean-square phase difference (structure function), which in turn depends on the spatial correlation function of ϕ (s) or, equivalently, on its wavenumber power spectrum. For example, under the Kolmogorov spectrum in the limit of small spatial offsets, the structure function $\propto s_d^{5/3}$, from which one finds that the characteristic scale for the field is proportional to wavelength to the inverse power 1.2 rather than 1.0 from our approximation.

The analysis in the Appendix, which assumes the limit of small spatial offsets, could be applied to a random variable as well as to a deterministic one and highlights the disagreement between the two approaches. The disagreement can be traced to the assumption of ergodicity in the screen phase, which supposes that a spatial average as in Equation (A5) converges to the same result as an ensemble average, as the limits of integration extend to infinity. Narayan & Goodman (1989) and Johnson & Narayan (2016) discussed various averaging regimes in VLBI observations. In practice the integration limits will be determined by the product of the transverse velocity times the observing time, yielding an “average image” for typical observing times. Thus short-term average estimators might be described by wavelength-scaling exponents near to $a = 2$ even for screens that have underlying phase spectra that follow a Kolmogorov wavenumber spectrum.

Apart from the different averaging regimes, the underlying plasma structures may also depart from the Kolmogorov power law. A simple case is Kolmogorov turbulence with dissipation at an inner scale l_{inner} , which could also lead to a wavelength exponent $a = 2$ when l_{inner} is greater than the half-width of the visibility function. However, the estimates of l_{inner} on lines of

sight to two pulsars by Spangler & Gwinn (1990) and Rickett et al. (2009) are less than a tenth of our visibility half-widths, making it unlikely that inner-scale effects play a role here.

Our finding of exponent a even less than 2 requires an alternative explanation, suggesting the screen truncation phenomenon, as proposed by Cordes & Lazio (2001). Their idea is that a limited extent of the scattering region, transverse to the line of sight (LOS), can restrict the angular width in scattered brightness. This could be analyzed in the spatial domain, using the method in the Appendix, with a restricted range in spatial extent s_m of the screen phase variations.

6.2. The Origin of Arclets

The other important feature of the scattered brightness is the presence of secondary peaks, significantly offset from the pulsar direction, that cause reverse arclets. The most notable secondary peak at 340 MHz is offset by 15 mas, 5.5 times further than the most notable one at 825 MHz, offset by 2.7 mas. By contrast, in our analysis of four sub-channels over 40 MHz bandwidth at 825 MHz, the center position of the arclet remained independent of frequency, although the detailed shapes changed substantially. Putting these results together shows that there are localized regions of enhanced scattering that remain identifiable, and slowly evolve, over a frequency range of at least 5%. However, they appear to decorrelate over an octave in frequency. They should be compared with bright peaks in the discrete reverse arcs of pulsar B0834+06, which have been observed to follow a precise frequency independence over a 10% bandwidth near 300 MHz (Hill et al. 2005; Brisken et al. 2010).

Frequency independence of the peaks strongly implies an origin from a specific location in the scattering region. The success of thin-screen models for the arcs is evidence for scattering plasma localized at discrete distance along the LOS; so, too, can there be enhanced local scattering transverse to the LOS. This could be due to relatively smooth lens-like plasma structures or a concentration of turbulent variations (i.e., intermittent turbulence). The 1D nature of the scattering suggests flattened plasma sheets aligned parallel to the LOS; the alignment would build up strong transverse phase gradients sufficient to cause lensing behavior or rapidly varying random phase variations, in either case causing discrete peaks in the scattered brightness. With local deviations in inclination of the plasma sheets, enhanced scattering peaks could originate where the sheets are accurately aligned with the LOS (Romani et al. 1987; Pen & Levin 2014; Simard & Pen 2018).

B0450–18 lies within ≈ 400 pc of the Earth and, when its position is plotted on a map of H- α emission, one can see faint curved structures that suggest nearby intersecting spherical shells such as the residuals of expanding supernovae. We suggest that such a shell, whose emission measure may be below the observable threshold in H- α , could be tangential to the LOS and cause the 1D arc scattering, and might even be located where the LOS intersects the plasma shell, thought to be the boundary of the Local Bubble. The electron density model of Yao et al. (2017) predicts the screen distance to be about 250 pc from the Earth.

7. Conclusion

In conclusion, we have observed a new highly anisotropic plasma condensation that is localized along the path from the

pulsar B0450–18. The frequency-scaling law of the scattered angular width has an exponent $a \approx 1.7 \pm 0.2$. It is significantly less than $a = 2.2$ expected for scattering from a Kolmogorov turbulent plasma. In that sense, it is reminiscent of many other pulsars with slower than expected frequency scaling in their pulse broadening times.

In its scattered profile, we also find narrower subsidiary offset peaks that cause discrete reverse arcs at both 340 and 825 MHz. The most prominent subsidiary peak at 825 MHz is independent of frequency over a narrow (5%) range, but its shape does evolve in detail. No prominent peak is observed at that angle at 340 MHz; there is a significant peak scattered at a 5 times greater angle and so cannot originate at the same physical location. The plasma responsible for the scattering appears to be localized in a thin “screen” that is highly anisotropic in its scattering properties.

We have also demonstrated agreement between two different techniques for estimating the scattered brightness, when the scattering is highly anisotropic.

Since the pulsar velocity is low, comparable to the Earth’s velocity, the curvature of the scintillation arcs would show strong annual variation. We plan follow-up arc observations over the course of a year, which will make use of the changing Earth velocity to constrain the screen distance and the orientation of the scattered image (Stinebring et al. 2005; Reardon et al. 2020).

We thank Daniel Baker for the development of `scintools.thtmod` (D. Baker et al. 2021, in preparation) used in our analysis. We thank Ue-Li Pen and Marten van Kerkwijk for useful discussions regarding θ - θ mapping implementation and precise curvature measurement. The θ - θ mapping is an original idea from Olaf Wucknitz, developed by Tim Sprenger, Daniel Baker, and others. Scott Ransom assisted with the observations and initial data processing, and we appreciate that help. This material is based upon work supported by the Green Bank Observatory which is a major facility funded by the National Science Foundation operated by Associated Universities, Inc. D.S. and H.Z. were funded by an NSF Physics Frontiers Center grant (1430284) to NANOGrav; they appreciate the support.

Appendix Scattering from a Phase Screen

Consider a fixed point source P located at $z = -z_p$ and transverse coordinate s_p . The phase screen lies at $z = 0$ and the observer O at transverse coordinate s_o is at a further distance $z = z_o$ where $z_o + z_p = L$.

The screen introduces a phase change $\phi(s_1)$ at transverse coordinate s_1 . Then the Fresnel diffraction integral for the complex field for an observer at $(s_o, z = z_o)$ can be written as

$$f(s_o, z = z_o) \simeq \frac{jk}{2\pi z_e} \exp[-jkL + j\Phi(s_p, s_o)] \times \int d^2s_1 \exp\left[j\phi(s_1) - j\frac{k|s_1 - s_{\text{eff}}|^2}{2z_e} \right]. \quad (\text{A1})$$

Here

$$\Phi(s_p, s_o) = k|s_p - s_o|^2/2L \\ s_{\text{eff}} = s_p z_o/L + s_o z_p/L, \quad (\text{A2})$$

where s_{eff} is the transverse coordinate where a straight line from P to O intersects the screen. $k = 2\pi/\lambda$ is the radio-frequency propagation constant; z_e is defined by $1/z_e = 1/z_o + 1/z_p$; the factor $jk/2\pi z_e$ ensures that the field at the observing plane has unit average intensity ($\langle ff^* \rangle = 1$).

The Fresnel integral Equation (A1) is a convolution of the electric field at the exit plane of the screen $f(s_o, z = 0)$ and the Fresnel propagator which is quadratic in phase. Thus it can also be written as a product in the Fourier domain, giving the angular spectrum of the field $F(\theta, z = z_o)$ versus the observed angle of arrival θ :

$$F(\theta, z = z_o) = F(\theta, 0) \exp[(jkz_e \theta^2)/2] \quad (\text{A3})$$

Here the angular spectrum emerging at the exit plane of the screen is

$$F(\theta, 0) = \int d^2 s_1 \exp[j\phi(s_1) + jk\theta \cdot s_1]. \quad (\text{A4})$$

Equation (A3) shows that propagation to an observer only changes the phase of the angular spectrum F , (see, for example, Ratcliffe 1956). The scattered brightness, introduced earlier, can be recognized as the squared magnitude of the angular spectrum F at the observer's plane. Hence $B(\theta)$ is independent of distance from the screen. The squared magnitude, Equation (A4), gives a double integral over s_1, s_2 , which can be re-expressed in terms of mean and difference spatial offsets $s_m = (s_1 + s_2)/2$ and $s_d = s_1 - s_2$. The result can be rearranged to show the well-known result that $B(\theta)$ is the Fourier transform of the visibility function of the field, where s_d is the baseline. Since this does not depend on the distance to the observer it is most convenient to write it at the exit plane of the screen. Hence:

$$\Gamma(s_d) = \int d^2 s_m \exp[j\phi(s_m + s_d) - j\phi(s_m - s_d)]. \quad (\text{A5})$$

Johnson & Gwinn (2015) identify the the Fourier transform of $\Gamma(s_d)$ as an ‘‘average’’ scattered image, where the integral is over a finite spatial range governed by the details of the observation. It is to be contrasted with an ensemble average, which leads to the familiar result that $\Gamma(s_d) = \exp[-0.5D_\phi(s_d)]$, where $D_\phi(s_d)$ is the structure function of phase—i.e., the mean of the squared phase difference on baseline s_d .

Equation (A5) allows us to consider how the scattered brightness function should scale with observing wavelength λ , since the screen phase is due to inhomogeneities in plasma density, whose well-known dispersion law makes the phase directly proportional to λ . Thus we write $\phi(s_m) = (\lambda/\lambda_0)\phi_0(s_m)$, where ϕ_0 is the screen phase at the reference wavelength λ_0 . In Figure 6 we displayed our models for $B(\theta)$ that were fitted to the observations at 340 and 825 MHz. We have also computed its Fourier transform to estimate the visibility functions $\Gamma(s_d)$ at each frequency, as shown in Figure A1.

Now consider the screen phase ϕ_0 as an unknown deterministic function, such as might apply in a lensing model, and examine how $\Gamma(s_d)$ might vary with wavelength. In Equation (A5) we now approximate ϕ_0 by a Taylor series to obtain

$$\Gamma_\lambda(s_d) = \int d^2 s_m \exp[j(\lambda/\lambda_0)s_d \cdot \nabla \phi_0(s_m) + O(s_d^2)] \quad (\text{A6})$$

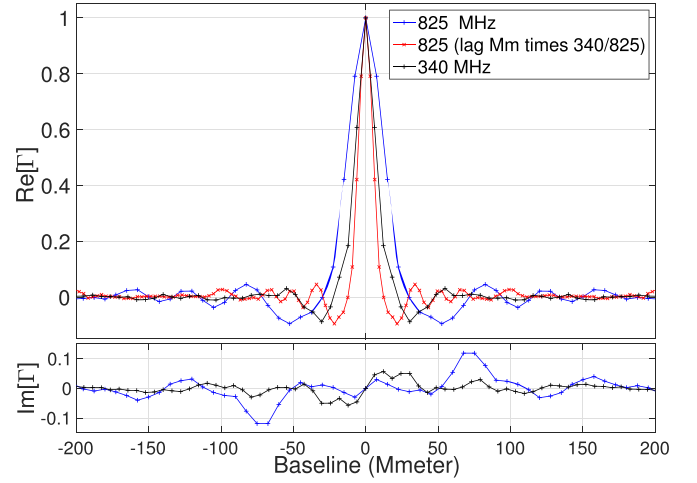


Figure A1. Real part of the visibility of the electric field (cosine Fourier transforms of the 1D brightness in Figure 6) at 340 MHz (black) and at 825 MHz (blue) vs. spatial offset in megameters and in red contracted spatially by the ratio 340/825.

$$\approx \Gamma_{\lambda_0}(s_d(\lambda/\lambda_0)). \quad (\text{A7})$$

In the final simplified form we only retain the first order in offset s_d and obtain the prediction that $\Gamma_\lambda(s_d)$ is a scaled version of Γ_{λ_0} , where the scaling makes the product $s_d\lambda$ a constant. Accordingly in the right panel of Figure 6 we have plotted the real part of $\Gamma_\lambda(s_d)$ for 340 (black) and 825 MHz (blue) and also over-plotted (red) 825 MHz scaled by the ratio of their wavelengths. The real part of Γ , which is the transform of the symmetric part of the brightness, dominates over the imaginary part. When the baseline scaled by the wavelength ratio, the scale at 50% for 825 MHz is somewhat narrower than that at 340 MHz, and corresponds to a wavelength exponent of -0.65 ± 0.2 . The fluctuations visible in the imaginary part of Γ provide an estimator for the error in the real part.

ORCID iDs

Barney J. Rickett <https://orcid.org/0000-0002-1138-2417>
 Dan R. Stinebring <https://orcid.org/0000-0002-1797-3277>
 Hengrui Zhu <https://orcid.org/0000-0001-9027-4184>
 Anthony H. Minter <https://orcid.org/0000-0002-6555-312X>

References

- Bhat, N. D. R., Cordes, J. M., Camilo, F., Nice, D. J., & Lorimer, D. R. 2004, *ApJ*, 605, 759
 Briskeen, W. F., Macquart, J.-P., Gao, J. J., et al. 2010, *ApJ*, 708, 232
 Chatterjee, S., Briskeen, W. F., Vlemmings, W. H. T., et al. 2009, *ApJ*, 698, 250
 Cordes, J. M., & Lazio, T. J. W. 2001, *ApJ*, 549, 997
 Cordes, J. M., & Lazio, T. J. W. 2003, arXiv:astro-ph/0301598
 Cordes, J. M., Rickett, B. J., Stinebring, D. R., & Coles, W. A. 2006, *ApJ*, 637, 346
 Geyer, M., & Karastergiou, A. 2016, *MNRAS*, 462, 2587
 Gupta, Y., Bhat, N. D. R., & Rao, A. P. 1999, *ApJ*, 520, 173
 Gwinn, C. R. 2019, *MNRAS*, 486, 2809
 Gwinn, C. R., & Sosenko, E. B. 2019, *MNRAS*, 489, 3692
 Hill, A. S., Stinebring, D. R., Asplund, C. T., et al. 2005, *ApJL*, 619, L171
 Jankowski, F., Bailes, M., van Straten, W., et al. 2019, *MNRAS*, 484, 3691
 Johnson, M. D., & Gwinn, C. R. 2015, *ApJ*, 805, 180
 Johnson, M. D., & Narayan, R. 2016, *ApJ*, 826, 170
 Lewandowski, W., Kowalińska, M., & Kijak, J. 2015, *MNRAS*, 449, 1570
 Löhmer, O., Kramer, M., Mitra, D., Lorimer, D. R., & Lyne, A. G. 2001, *ApJL*, 562, L157
 Löhmer, O., Mitra, D., Gupta, Y., Kramer, M., & Ahuja, A. 2004, *A&A*, 425, 569

- Narayan, R., & Goodman, J. 1989, *MNRAS*, **238**, 963
- Pen, U.-L., & Levin, Y. 2014, *MNRAS*, **442**, 3338
- Putney, M. L., & Stinebring, D. R. 2006, *ChJAS*, **6**, 233
- Ratcliffe, J. A. 1956, *RPPh*, **19**, 188
- Reardon, D. J., Coles, W. A., Bailes, M., et al. 2020, *ApJ*, **904**, 104
- Rickett, B., Johnston, S., Tomlinson, T., & Reynolds, J. 2009, *MNRAS*, **395**, 1391
- Romani, R. W., Blandford, R. D., & Cordes, J. M. 1987, *Natur*, **328**, 324
- Simard, D., & Pen, U.-L. 2018, *MNRAS*, **478**, 983
- Simard, D., Pen, U. L., Marthi, V. R., & Briskin, W. 2019, *MNRAS*, **488**, 4963
- Spangler, S. R., & Gwinn, C. R. 1990, *ApJL*, **353**, L29
- Sprenger, T., Wucknitz, O., Main, R., Baker, D., & Briskin, W. 2021, *MNRAS*, **500**, 1114
- Stinebring, D. R., Hill, A. S., & Ransom, S. M. 2005, in ASP Conf. Ser. 328, Binary Radio Pulsars, ed. F. A. Rasio & I. H. Stairs (San Francisco, CA: ASP), 349
- Stinebring, D. R., McLaughlin, M. A., Cordes, J. M., et al. 2001, *ApJL*, **549**, L97
- Stinebring, D. R., Rickett, B. J., & Koch Ocker, S. 2019, *ApJ*, **870**, 82
- Walker, M. A., Melrose, D. B., Stinebring, D. R., & Zhang, C. M. 2004, *MNRAS*, **354**, 43
- Walker, M. A., & Stinebring, D. R. 2005, *MNRAS*, **362**, 1279
- Yao, J. M., Manchester, R. N., & Wang, N. 2017, *ApJ*, **835**, 29